CLIMATOLOGY

Terrestrial amplification of past, present, and future climate change

Alan M. Seltzer[1]*, Pierre-Henri Blard[2,3], Steven C. Sherwood[4], Masa Kageyama[5]

Terrestrial amplification (TA) of land warming relative to oceans is apparent in recent climatic observations. TA results from land-sea coupling of moisture and heat and is therefore important for predicting future warming and water availability. However, the theoretical basis for TA has never been tested outside the short instrumental period, and the spatial pattern and amplitude of TA remain uncertain. Here, we investigate TA during the Last Glacial Maximum (LGM; ~20 thousand years) in the low latitudes, where the theory is most applicable. We find remarkable consistency between paleotemperature proxies, theory, and climate model simulations of both LGM and future climates. Paleoclimate data thus provide crucial new support for TA, refining the range of future low-latitude, low-elevation TA to $1.37^{+0.27}_{-0.23}$ (95% confidence interval), i.e., land warming ~40% more than oceans. The observed data model theory agreement helps reconcile LGM marine and terrestrial paleotemperature proxies, with implications for equilibrium climate sensitivity.

INTRODUCTION

The impact of future warming on human populations and ecosystems is primarily a function of regional changes. Consequently, it is imperative to understand mechanisms that lead to regionally divergent responses to ongoing and future climate change. Over recent decades, the land surface has warmed more than the sea surface in the low latitudes (*1*–*3*), and both transient and equilibrium climate model simulations ubiquitously predict that warming on land will continue to exceed sea surface warming (*1*, *3*–*7*). The mechanisms underlying terrestrial amplification (TA = land–to–sea surface warming ratio) are well understood to arise from fundamental thermodynamic differences between humid air over the ocean and drier air over land (*2*, *5*, *8*–*10*). However, natural variability, observational limitations, thermal lags, and non-CO_2 forcings preclude a precise estimate of TA from 20th century warming. For example, a recent analysis (*2*) found that warming over land has outpaced warming over oceans since the late 1970s by a factor of 1.42 ± 0.75 [95% confidence interval (CI)] between 40°S and 40°N. Narrowing the range of TA will aid in future predictions of low-latitude climate change, with relevance to both heat stress and water availability (*10*).

To evaluate predictions of TA, we extend a simple theory to the Last Glacial Maximum (LGM) to account for land-sea differences in low-latitude cooling. The LGM represents a useful test bed to evaluate theoretical TA predictions because the magnitude of warming from the LGM to preindustrial period greatly exceeds that since the start of the industrial revolution. We build upon prior efforts to explore the dynamical implications of the LGM land-sea temperature contrast (*11*, *12*), enabled both by theoretical advances (*2*, *5*) and recent proxy constraints on low-latitude land- and sea surface temperatures during the LGM (*13*, *14*). LGM paleotemperature proxy insights into TA can, in turn, be used to inform future predictions using by optimizing the TA theory, yielding a range of TA values that can be directly compared with global circulation model (GCM) simulations of future warming. In this study, we evaluate LGM proxy–informed predictions of TA under enhanced greenhouse warming and compare with recent GCM simulations under elevated atmospheric CO_2 concentrations (*15*). We focus our analysis on the low latitudes (defined here as 30°S to 30°N) at low elevation (below 1 km), because this is where the dynamical assumptions underpinning this theory are best justified. The low latitudes also play an outsize role in impacting global climate (*16*), and the absence of LGM glaciation in this region also facilitates a more direct comparison with recent and future climate change.

RESULTS AND DISCUSSION

Theoretical framework

We adopt the moist static energy (MSE) theory of Byrne and O'Gorman (*2*)—hereafter, BO18—to TA. In particular, we extend this theory to account for the climate state of the LGM, when eustatic sea level was ~120 m lower than present (*17*, *18*). The core concept underpinning of the BO18 theory is that atmospheric circulation in the low latitudes, where the Coriolis force is weak, acts to efficiently homogenize changes in temperature aloft, leading to corresponding changes in near-surface MSE via convective adjustment (Fig. 1). Consequently, under global warming or cooling, changes in MSE over the land and sea surfaces in the low latitudes should be effectively equal, on average, over large spatial scales. Formally, this underlying prediction is stated as follows

$$\Delta h_L = \Delta h_O \quad (1)$$

where h (J kg^{-1}) is near-surface MSE, the subscripts L and O refer to land and ocean in the low latitudes, respectively, and Δ indicates a change from preindustrial climate. Changes in MSE can arise from changes in three components—temperature, moisture, and elevation—as stated in the following definition

$$\Delta h = c_p \Delta T + L_v \Delta q + g \Delta z \quad (2)$$

[1]Department of Marine Chemistry and Geochemistry, Woods Hole Oceanographic Institution, Woods Hole, MA, USA. [2]Centre de Recherches Pétrographiques et Géochimiques, CNRS, Université de Lorraine, Vandoeuvre-lès-Nancy, France. [3]Laboratoire de Glaciologie, Université Libre de Bruxelles, Brussels, Belgium. [4]Climate Change Research Centre, University of New South Wales, Sydney, New South Wales, Australia. [5]Laboratoire des Sciences du Climat et de l'Environnement/Institut Pierre-Simon Laplace (LSCE/IPSL), UMR CEA-CNRS-UVSQ, Université Paris-Saclay, Gif-sur-Yvette, France.
*Corresponding author. Email: aseltzer@whoi.edu

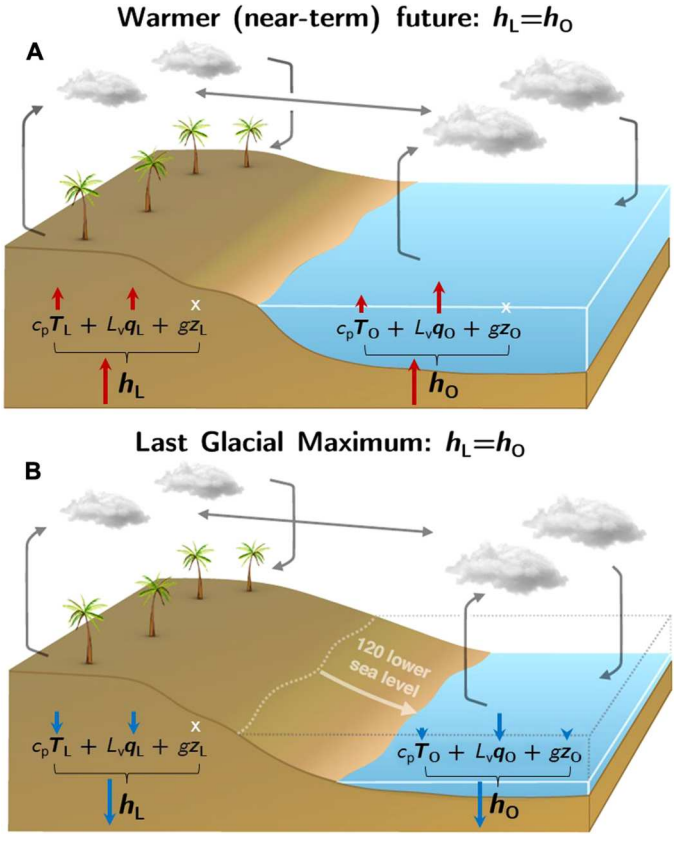

Fig. 1. Illustration of land and sea surface changes in MSE and its components. (**A**) Changes in MSE (h) under near-term warming, relative to modern climate. (**B**) Changes in MSE for LGM cooling, relative to modern climate. Red and blue arrows represent the relative magnitudes of change in each MSE component relative to the preindustrial era (X indicates no change), where red/up indicates an increase and blue/down indicates a decrease. MSE changes (either positive or negative under warming or cooling, respectively) in the low altitudes are, by theory, equal in magnitude over ocean and over land due to convective adjustment to horizontally uniform changes in temperature aloft as represented by the gray arrows. Note that warming scenario (top) considers only near-term warming accompanied by a minor rise in sea level relative to the 120-m drop in sea level during the LGM.

where c_p is the specific heat capacity of air at constant pressure (J kg^{-1} K^{-1}), T is near-surface air temperature (K), L_v (J kg^{-1}) is the latent heat of vaporization of water, q is near-surface specific humidity (kg^{-1} kg^{-1}), g is gravitational acceleration (m s^{-2}), and z is geopotential height (m) (i.e., elevation, defined with respect to preindustrial sea level in this study).

A second key advance by the BO18 model is to note that changes in land surface and sea surface specific humidity should be proportional and that this constant of proportionality, γ, should hold under climatic warming or cooling

$$\Delta q_L = \gamma \Delta q_O \tag{3}$$

The assumption of constant γ is rooted in a box-model analysis demonstrating that, under the assumptions that changes in vertical and horizontal mixing time scales are proportional and that changes in boundary-layer heights over land and ocean are small under global warming, changes in γ should be small (*7*). Notably, the expectation for a relatively constant γ has also independently been shown by a separate conceptual model and Lagrangian air mass analysis (*19*). Observations and climate model simulations suggest that γ is ~0.7 between 40°S and 40°N but with large uncertainties and regional variability (*2*, *7*). Here, we use recent paleotemperature constraints from the LGM to refine this estimate of γ. In this study, to determine Δq_O, we account for the nonlinear temperature dependence of saturation vapor pressure (*20*), the slight impact of higher LGM sea surface pressure (*14*, *21*) on q_O, and a small change in ocean near-surface relative humidity (RH) with warming or cooling (0.54 ± 0.28% K^{-1}) as suggested by GCM simulations (Methods).

By combining Eqs. 1 to 3, given that $\Delta z_L = 0$ for the LGM[16], we can derive an expression for ΔT_L as a function of ΔT_O under climatic warming or cooling

$$\Delta T_L = \Delta T_O + \left(\frac{L_v}{C_p}\right)\Delta q_O(1-\gamma) + \left(\frac{g}{c_p}\right)\Delta z_O \tag{4}$$

For the LGM, the 120 m lowering of sea level must be accounted for in Eq. 4. Crucially, air pressure in the LGM atmosphere as a function of geopotential height was approximately unchanged from the present (*21*) because the lowering of global sea level was compensated by displacement of air due to the growth of large ice sheets in the high latitudes. Consequently, barometric pressure at a fixed point on land at low elevation and low latitude was the same as today during the LGM, whereas barometric pressure at the LGM sea surface was higher than present by ~15 hPa (*14*, *21*). This means that the maritime LGM cooling on a constant geopotential surface is greater than that at the sea surface (indicated by proxies). Note that the difference is not simply governed by the dry adiabatic lapse rate (e.g., third term on the right-hand side of Eq. 4) but rather by coupled changes in temperature and moisture. For example, even for $\Delta h = 0$, a change in sea level Δz_O would lead to a corresponding compensatory change in sea surface humidity Δq_O, causing both the second and third terms in Eq. 4 to change. However, for ongoing and future centennial-scale warming, changes in the third term of Eq. 4 can be neglected [as in (*2*)] because the contribution of changes in geopotential height due to sea level rise are small relative to changes in temperature and specific humidity. Thus, ongoing and future TA is controlled exclusively by the first two terms on the right-hand side of Eq. 4.

TA in the LGM

By extending the BO18 framework to account for sea level change, we can draw insights into low-latitude TA from paleoclimate proxy data and model simulations of the LGM (*22*). We first consider how paleoclimate data from the low-latitude, low-elevation land surface and sea surface inform dynamical land-sea coupling of moisture changes (i.e., γ in the BO18 theory). In previous studies, γ has been determined via ratios of land surface– and sea surface–specific humidity in observations and models in the low latitudes (*2*, *7*). However, idealized model simulations of γ vary markedly from full climate model simulations (*7*), and so the use of LGM proxy data presents an opportunity to independently constrain γ from a vastly different climate state.

To estimate γ in the LGM, we draw on two recent, independent compilations of low-latitude terrestrial and marine paleotemperature proxy data from the LGM. The marine reconstruction (*13*)

uses a large dataset of geochemical proxies with well-established statistical proxy system models to estimate ocean cooling during the LGM via data assimilation, finding a 3.5° ± 0.3°C (95% CI) cooling of the low-latitude sea surface. The terrestrial reconstruction (*14*) compiles records of dissolved noble gases in groundwater and applies a unified physics-based model to quantitatively resolve solubility-controlled signals of LGM land surface cooling at low elevation in the low latitudes, equatorward of mid- to high-latitude regions influenced by the large LGM ice sheets, finding 5.8° ± 0.6°C (95% CI) of low-latitude land surface cooling. While this estimate spans a somewhat larger range of latitude (45°S to 35°N), the mean LGM cooling suggested by noble gas records between 30°S and 30°N [5.9° ± 0.8°C, 95% CI; (*14*)] is spatially constant within uncertainty. We do not include continental paleotemperature records located at elevations higher than 1000 m, given that complex spatiotemporal changes in the lapse rate (*23*–*25*) preclude direct application of the BO18 theory.

Using these estimates of ΔT_O and ΔT_L, we rearrange Eq. 4 to solve for γ and generate 10^6 Monte Carlo simulations of the other quantities to account for uncertainties in proxy data, sea level, modern temperature, specific humidity, and changes in ocean surface RH with temperature (Fig. 2 and Methods). We find a mean proxy-implied γ value of 0.84 (95% CI, 0.73 to 0.94). This is somewhat higher than the modern observation-based value [0.72; (*2*)], and we suggest that investigating the potential processes associated with this apparent difference may improve our future understanding of TA. For the purpose of the present study, however, we note that this result is still unambiguously consistent with the notion that $\Delta q_L < \Delta q_O$, which implies that TA in the LGM occurred due to changes in both moisture and sea level.

In Fig. 3, we compare proxy-based BO18 theory predictions of low-latitude TA to LGM land surface and sea surface cooling in Paleoclimate Modeling Intercomparison Project 4 (PMIP4) LGM simulations (*22*) between 30°S and 30°N and below 1-km elevation. We note that a small correction was required due to insufficient lowering of LGM sea level across PMIP4 models, which leads to a slight cooling of the sea surface (Methods).

We find that TA is ubiquitous across all PMIP4 models, in line with previous LGM model studies (*12*, *26*, *27*). Using Eq. 4, we also show expected land surface and sea surface cooling for a range of different γ values. We find that 10 of 13 models agree with the proxy-informed γ estimate within error despite different magnitudes of land surface and sea surface cooling. Similarly, the high correlation of ΔT_O and ΔT_L (r = 0.95) across this wide range of model estimates of LGM cooling suggests that TA is governed by a single common mechanism despite complex intermodel differences in atmosphere-ocean-cryosphere dynamics. This analysis of the BO18 theory under the LGM conditions shows that this theory is equally applicable under different climate states.

This theoretical framework provides a new physical basis to evaluate paleotemperature proxy estimates of LGM cooling. For example, we find that two prior compilations of marine (*28*) and terrestrial (*29*) proxy data, which include species assemblage data and indicate less overall LGM cooling, are theoretically compatible with each other (γ between 0.8 and 0.9; Fig. 3). However, interchanging these previous species assemblage–based estimates (*28*, *29*) with more recent geochemical compilations (*13*, *14*) would lead to unphysical results: γ > 1 [by combining assemblage-based ΔT_L (*29*) and geochemical ΔT_O (*13*)] or γ < 0.5 [by combining noble gas-based ΔT_L (*14*) and assemblage-based ΔT_O (*28*)]. The requirement that specific humidity changes are larger over the ocean implies that γ < 1, and models and observations (*2*, *7*) rule out γ as low as 0.5. We note that recent improvements in quantitative reconstruction of temperature from plant species assemblage data have led to increased estimates of low-latitude LGM cooling, including a revised estimate of ~5°C from the pollen data (*30*). To refine estimates of LGM cooling that inform determinations of equilibrium climate sensitivity (ECS) (*13*, *31*, *32*), this theoretical foundation

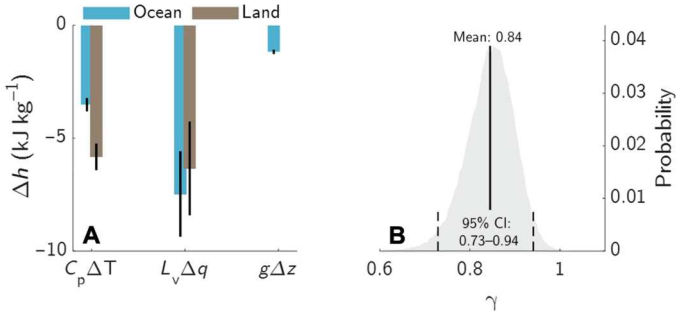

Fig. 2. Components of BO18 theory for LGM cooling informed by paleotemperature proxies. (**A**) Decomposition of LGM (versus preindustrial) changes in individual MSE components over land and ocean in the low latitudes. (**B**) Probability distribution function of γ constrained by LGM paleotemperature proxy data. Using marine (*13*) and terrestrial (*14*) proxy compilations, we find a mean γ value of 0.84 (95% CI, 0.73 to 0.94) for the LGM in 10^6 Monte Carlo simulations to account for uncertainties in paleoclimate data and model parameters (Methods). Error bars in (A) represent 95% CIs.

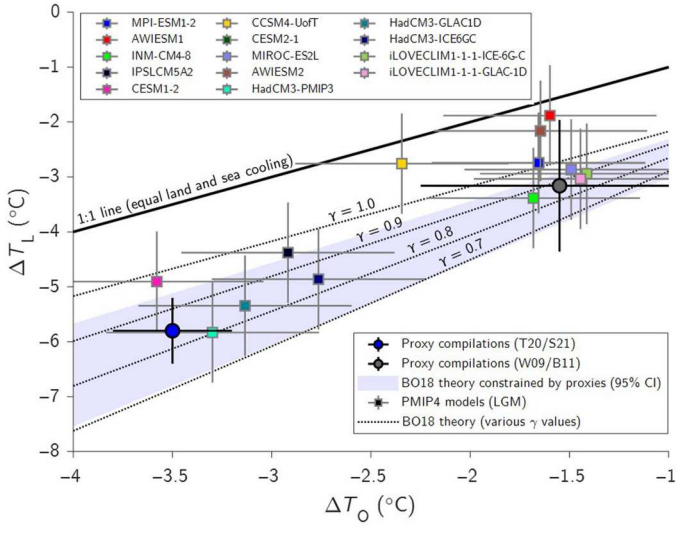

Fig. 3. Amplified cooling over land surfaces during the LGM. Comparison of relationships between 30S° and 30°N LGM land and sea surface cooling, ΔT_L and ΔT_O, across PMIP4 LGM simulations (squares), recent geochemical proxy constraints (*13*, *14*) (blue circle: T20/S21), prior compilations of species assemblage and geochemical proxies (*28*, *29*) (gray circle: W09/B11), and BO18 theoretical predictions with γ values either shown (dashed lines) or informed by geochemical proxies (*13*, *14*) (blue shaded 95% confidence region). Error bars on proxy data represent 95% CIs, and error bars on model simulations reflect regional variability for comparison with proxies (±2σ range of differences between 30S° and 30°N mean values and resampling at ocean and land proxy locations).

represents a crucial step toward reconciling disparate estimates of LGM cooling by integrating a multitude of compatible proxies to improve spatial coverage and reduce uncertainty.

To inform our comparison between paleotemperature proxy and model data, we carried out a sensitivity test, selecting model grid points nearest to locations of marine (*13*) and terrestrial (*14*) proxy data. We then compared the mean cooling across selected grid points to the low-latitude mean cooling over land and ocean surfaces. We find proxy location mean minus low-latitude mean cooling differences over ocean and land to be −0.2° ± 0.5°C (2σ) and − 0.5° ± 0.9°C (2σ), respectively, and we adopt these intermodel variabilities as model error estimates in Fig. 3. We suspect that the three outlying models (γ > 1) may be affected by anomalous adiabatic land surface warming and sea surface cooling associated with high land surface pressure and low sea surface pressure, respectively, related to the prescribed LGM sea level change. The limited available surface pressure data supports this notion (fig. S1 and Methods). We exclude the Community Earth System Model 2 LGM simulation from Fig. 2 because of its known bias toward unrealistically large LGM cooling (*33*) (for completeness, it is included in fig. S2 and does not invalidate the γ and TA estimates).

An important finding of this analysis is that a γ value of ~0.7 [based on modern observations (*2*) but with considerable uncertainty] would imply an LGM land surface cooling of ~7.5°C associated with the 3.5°C sea surface cooling suggested by geochemical proxies (*13*). This is substantially greater than the 5.8°C constraint from terrestrial noble gas data (*14*), suggesting that projections of future TA, assuming that γ = 0.7, may be too extreme, although we note that the BO18 theory is only expected to hold for the large-scale mean, so it does not preclude some regional variability in TA at individual proxy sites. While there is considerable scatter among the PMIP4 LGM simulations (Fig. 3), all models suggest γ > 0.8, in agreement with the LGM temperature paleotemperature proxies (Fig. 3 and fig. S2). Thus, LGM paleotemperature proxy and model data would imply somewhat weaker TA in the future than predictions based on modern observations.

Paleoclimate insights into future TA

To test this expectation, we compare theoretical predictions of TA informed by LGM proxy data ($\gamma = 0.84^{+0.10}_{-0.11}$; 95% CI), with land surface and sea surface warming in climate model simulations forced by elevated greenhouse gas concentrations. Here, we explore the magnitude of low-latitude land and ocean surface warming across multiple models in two Coupled Model Intercomparison Project 6 (CMIP6) scenarios (*15*, *34*). The first is Shared Socioeconomic Pathway (SSP) 5-8.5, which is a high fossil fuel emission scenario (*15*, *35*) in which the global anthropogenic greenhouse gas radiative forcing reaches 8.5 W m^{-2} by 2100. The second scenario (4×CO_2) involves an instantaneous quadrupling of the atmospheric CO_2 concentration, relative to the preindustrial era, and this elevated concentration is sustained for 150 years of model simulation (*15*). For the SSP5-8.5 scenario (32 models) and 4×CO_2 scenario (17 models), we calculated ΔT_L, ΔT_O, and changes in land and ocean RH between 30°S and 30°N (Methods and tables S2 and S3). Figure 4 shows a comparison of land surface and sea surface warming in these 17 CMIP6 model simulations alongside predictions from the BO18 with different γ values, including the LGM proxy–informed range.

Despite large intermodel differences in the magnitude of low-latitude warming for each scenario, we find consistent land-sea warming ratios, with mean values of 1.45 ± 0.12 (2σ) and 1.49 ± 0.21 (2σ) for the 4×CO_2 and SSP5-8.5 scenarios, respectively. Using the BO18 theory constrained by LGM proxies, for 2°C of ocean-surface warming, we find $2.73^{+0.55}_{-0.46}$°C of land surface warming, equivalent to a mean TA value of $1.37^{+0.27}_{-0.23}$ (95% CI). This value is slightly below the CMIP6 model scenarios, but all three estimates agree within error. We carried out a sensitivity test in which LGM proxy data were used to inform TA assuming no change in RH over oceans, which led to a mean TA value of 1.36, virtually identical to the result obtained if a 0.57% K^{-1} increase in RH is prescribed (Methods). Both the CMIP6 simulations and LGM-informed theory predictions of TA agree closely with the 1.42 ± 0.75 (95% CI) value suggested by recent observations (*2*) in the low latitudes (between 40°S and 40°N). Our analysis, however, permits us to substantially reduce the uncertainty associated with this TA estimate, refining the extremely likely (95% CI) low-latitude range to ~1.2 to 1.6. Thus, three independent lines of evidence, from paleoclimate proxies, GCM simulations of future warming, and modern observations, all suggest that the low-latitude land surface will warm, on average, by ~40% more than the sea surface. The consistency in simulated and theory-predicted TA between models and across climate states notably provides support for the expectation of a relatively climate-state independent γ value that is below unity (*7*, *19*). This suggests that despite large intermodel scatter in simulated future warming owing to complex dynamical differences between models, the low-latitude coupling of moisture and heat is indeed well represented by the simple BO18 theory. The agreement between LGM-informed BO18 theory and CMIP6 simulations of future warming therefore provides confidence in climate model predictions of TA, even in models for which simulation of other dynamical parameters is less robust.

This low-latitude TA estimate is somewhat lower than global mean TA values of 1.5 to 1.6 suggested by GCM simulations of future warming (*1*, *3*), but it is consistent with past model-based indications of lower TA in the low latitudes (*1*). There are several possible reasons for these differences. The BO18 theory relies on dynamical properties of the low latitudes (convection and weak Coriolis force) and is consequently less applicable at mid and high latitudes. Polar amplification also plays a large role in accentuating land warming in the high latitudes. Recent MSE balance approaches to understanding polar amplification (*36*) might be paired with the BO18 theory in future studies of global-scale TA. In this study, however, we restrict our analysis to the low latitudes and low elevation, where the BO18 theory is applicable in a simple and straightforward way. This analysis is, to our knowledge, the first to demonstrate that simple thermodynamic expectations for TA are equally valid under past, present, and future climate change.

Implications and outlook

Our findings have implications for the validity of simple theory predictions across a wide range of climate states and for fundamental expectations about past climate that are of relevance to future terrestrial-marine interproxy comparisons, paleoclimate model-data evaluation, and paleoclimate constraints on Earth's ECS. The consistency of theoretical expectations for TA both in a colder past and warmer future, supported by paleoclimate proxy evidence and

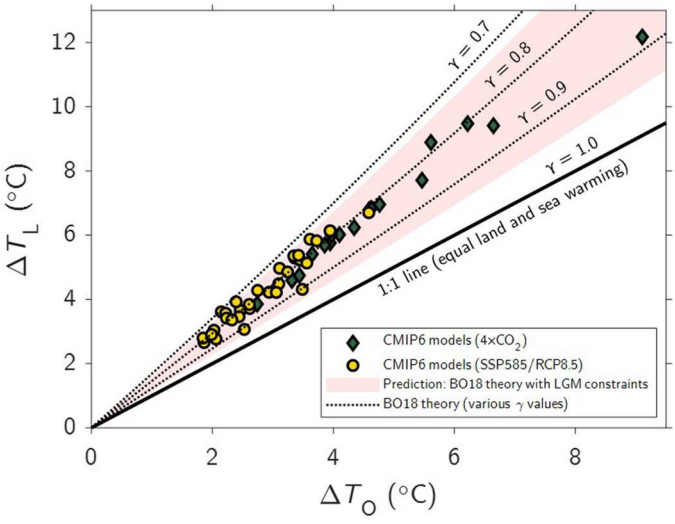

Fig. 4. Amplified warming over land surfaces under elevated greenhouse gas concentrations. Warming of the low-latitude (30°S to 30°N) land and sea surface in CMIP6 simulations for an abrupt quadrupling of CO_2 (green diamonds; 4×CO_2) and under the SSP5-8.5 emission scenario (yellow circles). The 4×CO_2 data (17 models) reflect the final decade of the simulation (141 to 150 years after start) relative to preindustrial era. The SSP585/RCP8.5 data (32 models) reflect the difference between year 2085 to 2099 and 2015 to 2029 means. The red shaded region represents BO18 theoretical predictions using independent constraints from LGM proxy data (95% CI). Dashed lines represent BO18 theoretical predictions of land surface and sea surface warming under different γ values.

GCM simulations, adds confidence to future predictions of land-sea differences under future warming. These LGM-informed results are most applicable to the low latitudes at low elevation, where billions of people may be affected by future changes in heat stress and water availability. In addition to TA, the BO18 theory sheds light on future changes in moisture over land. For example, using the BO18 theory, our results suggest that for 2°C of ocean surface warming in the low latitudes, land surface RH will decrease by $1.9^{+1.5}_{-1.7}$% (95% CI), which agrees with CMIP6 model simulations (fig. S3). These predicted changes in hydroclimate are useful for policymakers in planning for adaptations to future climate change. While there are regional exceptions to these expectations [for example, at high elevation, in regions subject to significant changes in the position of the intertropical convergence zone (*37*, *38*) and in regions of weaker convection], this analysis and the theory it is based on provide an important foundation for large-scale mean changes in temperature and moisture in the low latitudes under ongoing and future warming.

Our study has also several possible implications for studies of past climate and for paleoclimate estimates of ECS. First, in light of consistent evidence from models, paleoclimate proxies, and theory, it is important for terrestrial-versus-marine proxy intercomparisons to account for TA. In doing so, future efforts to synthesize proxy estimates of LGM cooling from land and sea will have a stronger basis upon which to assess the compatibility of individual records, providing a path toward improved multiproxy reconstructions that will reduce uncertainties in LGM cooling and corresponding estimates of ECS. While there is an understandable tendency to adopt the null hypothesis that the low-latitude, low-elevation land surface would have warmed or cooled by the same magnitude on average as the nearby sea surface, it seems reasonable to expect that, in general, (paleo)temperature change is amplified over land surfaces. This concept is not original, and, indeed, the compatibility (or lack thereof) between terrestrial and marine proxy records of LGM cooling has raised dynamical questions about land-sea coupling for decades (*11*, *12*). However, with major progress led by the atmospheric dynamics community in understanding future and present land-sea warming ratios, there is now an opportunity to establish a robust framework for TA in the past. We suggest that BO18 theory provides a simple, accessible, physics-based approach to consider past changes in TA, and we advocate for its adoption in future paleoclimate studies.

Second, for LGM proxy-model intercomparison and LGM-based estimates of ECS, this study points to the importance of adiabatic warming induced by elevated barometric pressure as a potentially important factor to consider. Because this warming is not climatic in origin—that is, it is a unique product of increased LGM ice volume and thus not of direct relevance for 21st century warming—we suggest that correcting for it would improve LGM estimates of ECS. For example, assuming conservation of MSE over the sea surface and adopting values of ~12°C for global mean LGM sea surface temperature and 75% RH over oceans, a 120-m lowering of sea level would directly warm the sea surface by ~0.6°C, independent of any climatic forcing (Methods). Because oceans represent ~70% of the global surface area, correcting for this nonclimatic warming would enhance the magnitude of LGM global mean surface cooling by ~0.4°C. Inclusion of this correction would have an appreciable impact on ECS determinations based on LGM cooling (*13*, *32*, *39*, *40*), and it is thus important for future studies to account for this effect.

Last, from a broader perspective, this study presents an approach by which paleoclimate constraints may be used to inform future climate change. We advocate for future studies to leverage paleoclimate data and simple dynamical theories to capitalize on the promise of paleoclimate science, namely, to draw on insights into vastly different past climate states, well beyond the short instrumental record, to shed light on how our planet may change in the future.

METHODS

Determination of γ from LGM proxy data

To estimate γ and its uncertainty from LGM paleotemperature proxy constraints between 30°S and 30°N, we rearranged Eq. 4 to solve for γ and carried out 10^6 Monte Carlo simulations for uncertainty analysis. This exercise also facilitated the determination of changes in individual MSE components and their associated uncertainties (Fig. 2). To determine Δq_O, we assume a preindustrial 30°S to 30°N ocean mean surface air temperature of 24° ± 1°C (±2σ), which is 0.5°C below the 1959 to 2021 mean ERA5 reanalysis surface air temperature over oceans across this latitude range (*41*). We assume a mean preindustrial era near-surface RH over oceans of 0.78 based on ERA5 reanalysis (*41*), and we adopt a 2σ uncertainty of ±0.02. Physical constants of g = 9.8 m s^{-1}, C_p = 1005 J kg^{-1} K^{-1}, and $L_v = 2.453 \times 10^6$ J kg^{-1} are adopted, and uncertainties in these values are assumed to be negligible.

We calculate Δq_O by subtracting q_O for the LGM ($q_{O,LGM}$) from q_O for the preindustrial era ($q_{O,PI}$). Specific humidity, q, is defined as

follows

$$q \equiv \frac{m_w}{m} = \frac{w}{w+1} \quad (5)$$

where m_w and m refer to the mass of water vapor and total air per unit volume, respectively, and w is the mass mixing ratio of moist air to dry air (i.e., $w \equiv m_w/m_d$, where m_d is the mass of dry air per unit volume). We calculate w as follows

$$w = \frac{M_w e_{sat}(T)\mathrm{RH}}{M_d P_s} \quad (6)$$

where M_w and M_d are the molar masses of water vapor (0.018 kg mol^{-1}) and dry air (0.029 kg mol^{-1}), respectively, e_{sat} is the saturation vapor pressure (hPa) at temperature T parameterized in (*20*), and P_s is surface air pressure (hPa). Using the preindustrial values given above, $q_{O,PI}$ = 0.0138 kg kg^{-1}. Thus, for a given LGM sea surface cooling (ΔT_O) and accounting for the increase in surface pressure over the lower LGM sea surface (*21*), Eq. 1 and Eq. 2 can be used to determine Δq_O and solve for γ via Eq. 4.

Our determination of Δq_O assumes a slight change in near-surface (RH) over oceans with warming or cooling based on both model simulations (*17*) and theoretical considerations. In CMIP6 SSP5-8.5 simulations, between 30°S and 30°N, we find a mean change in RH with temperature over oceans of 0.54 ± 0.28% K^{-1} (2σ) across the 32 models analyzed in this study. Note that we report RH in absolute percentage, such that a 1-K warming, for example, would increase mean RH over oceans from 0.78 to 0.7854. This is consistent with predicted fractional changes in global evaporation rates of ~1 to 2% K^{-1} from models and theory (*42*). That is, because evaporation scales with both (1-RH) and saturation-specific humidity (q_S), and q_S over low-latitude oceans increases fractionally by ~6% K^{-1} via the Clausius-Clapeyron relation, (1-RH) should decrease fractionally by ~4% K^{-1} with warming assuming small change in the bulk heat transfer coefficient. Because preindustrial (1-RH) over low-latitude oceans is ~0.2 (i.e., 1 to 0.78), the expected increase in RH with warming is ~0.2 times the fractional change in (1-RH) with warming, that is, ~0.005 to 0.01 K^{-1}, which is in line with the model values. In light of these considerations, we adopt the mean RH temperature sensitivity of the CMIP6 SSP5-8.5 models in this analysis. We also carried out a sensitivity test in which RH over oceans is constant under warming or cooling, which led to negligible changes in mean TA and γ. We report and discuss the results of this sensitivity test in the main text.

For the proxy-based Monte Carlo determination of γ, we adopt the following LGM versus preindustrial changes between 30°S and 30°N: $\Delta T_L = -5.8° \pm 0.6°C$ (*14*), $\Delta T_O = -3.5° \pm 0.3°C$ (*14*), and $\Delta z_O = -120 \pm 5$ m (*17*, *18*) (all uncertainties are ±2σ, and observational errors are assumed to be statistically independent and normally distributed). We note that the land surface paleotemperature constraint spans a slightly wider range of latitudes, but we emphasize that there is no significant trend with latitude across all records equatorward of LGM ice sheet influence (i.e., 45°S to 40°N). The mean ΔT_L value from noble gas records between 30°S and 30°N is −5.9°C (*14*). While changes in relative sea level likely led to spatial heterogeneity in the Δz_O throughout the low latitudes in the LGM, for the low-latitude focus of this study, we assume that the 30°S to 30°N mean LGM sea level change was equal to the global mean sea level change of ~120 m. A recent global sea level reconstruction (*18*) indicates that the 30°S to 30°N mean change in LGM sea level was within 1 m of the global mean change.

Analysis of CMIP6/PMIP4 model data

To determine the magnitude of ΔT_L and ΔT_O from GCM simulations, we compared mean annual surface air temperatures in PMIP4 LGM experiments (*22*) and CMIP6 4×CO_2 experiments to preindustrial control experiments. As described in the main text, CMIP6 SSP5-8.5 ΔT_L and ΔT_O represent differences between 2085 to 2099 and 2015 to 2029. For each model, of ΔT_L and ΔT_O reflect area-weighted mean surface air temperature changes over land and ocean grid cells, respectively, between 30°S and 30°N. For LGM experiments, we computed averages of publicly available monthly mean climatologies (*22*), and for 4×CO_2 and SSP5-8.5 experiments, we calculated annual mean surface temperatures for the time intervals described above. Note that the final 10 years of the 150-year 4×CO_2 experiments were averaged, which appears to capture the equilibrium warming response (fig. S4).

We apply small corrections (order 0.1°C) to ΔT_O from LGM PMIP4 simulations for anomalous cooling associated with higher-than-expected LGM sea surface. In fig. S5, we show changes in the orography variable ("orog": surface altitude relative to global mean sea level) averaged over 30°S to 30°N land and sea surfaces. Because the 30°S to 30°N LGM change in sea level is known to have been nearly identical to the global mean (*18*), we expect Δorog over oceans in PMIP4 models to be ~0, which is indeed the case (mean across PMIP4 models = −0.44 m; fig. S5). Because that absolute elevation of the low-latitude land surface was unchanged in the LGM, we expect that Δorog over land should be ~120 m, reflecting the lower LGM sea level. However, we find that all PMIP4 models show Δorog <120 m over land, with an intermodel mean value of ~70 m (fig. S5). We correct for the anomalous sea surface cooling associated with high-biased LGM sea level via conservation of MSE (Eq. 2), which results in a correction of 0.0038°C m^{-1}, leading to a mean correction of 0.19°C across the PMIP4 models. Surface pressure data were available for five PMIP4 LGM simulations and confirm that the LGM sea surface pressure increased by less than expected [i.e., <15 hPa (*21*)] over oceans but remained constant over land in most models. However, there are two notable exceptions. First, in the MIROC-ES2L model, no change was made to LGM sea level (Δorog over land = 0; fig. S5), which leads to anomalously high surface pressure over land (i.e., $\Delta P_S > 0$ hPa) and anomalously low surface pressure over oceans (i.e., $\Delta P_S < 15$ hPa; fig. S1). We correct for the corresponding warm bias in land temperature and cold bias in ocean temperature in the same manner as above, such that MSE is conserved. Second, in the AWIESM1 model (and likely the AWIESM2 model, although no data are available), land surface pressure is anomalously high and sea surface is anomalously low despite a change in sea level (Δorog over land = 87.8 m for both AWI models). We do not attempt to correct land surface temperature in these models, but we note that AWIESM1 and AWIESM2 represent two of the three models that do not conform to the BO18 theory expectations (Fig. 3), and we note that the land and ocean temperature biases associated with these surface pressure biases are indeed of an appropriate sign and magnitude to explain the deviation of these models from the BO18 theory predictions. All individual PMIP4/CMIP6 model ΔT_L and ΔT_O values are provided in tables S1 and S2, respectively.

Impact of sea level lowering on global mean sea surface temperature

For the purposes of improved ECS determination and proxy-model comparison, we consider a hypothetical example in which global mean LGM temperature and RH over the ocean are 12°C and 75%, respectively, before sea level is lowered by 120 m. This allows us to estimate the (nonclimatic) warming of the LGM sea surface due to lower sea level alone. By conservation of MSE (i.e., $\Delta h = 0$), a 120-m lower LGM sea level ($\Delta z = -120$) must lead to higher T_O and q_O. Formally, by rearrangement of the MSE equation, ΔT_O (the ocean warming induced by sea level change alone) can be determined as follows

$$\Delta T_O = -\frac{g\Delta z}{C_p + L_v q_o \alpha / 1.015} \quad (7)$$

where q_O is the global mean specific humidity over the ocean (0.0063 kg kg^{-1}) and α is the linearized change in saturation vapor pressure with temperature (~6.8% K^{-1}) (*20*). This equation accounts for the direct effect of lower sea level on specific humidity (a ~1.5% lower specific humidity due to ~15-hPa higher-surface air pressure above the lower LGM sea surface (*21*)].

Using Eq. 7, we find that a 0.58°C warming is induced by a 120 m lowering of the LGM sea surface. The result is rather insensitive to the assumed initial global mean sea surface temperature. For example, assuming a 10° or 14°C initial temperature leads to ΔT_O values of 0.62° and 0.54°C, respectively.

Supplementary Materials

This PDF file includes:

Figs. S1 to S5
Tables S1 to S3
References

REFERENCES AND NOTES

1. R. T. Sutton, B. Dong, J. M. Gregory, Land/sea warming ratio in response to climate change: IPCC AR4 model results and comparison with observations. *Geophys. Res. Lett.* **34**, (2007).
2. M. P. Byrne, P. A. O'Gorman, Trends in continental temperature and humidity directly linked to ocean warming. *Proc. Natl. Acad. Sci. U.S.A.* **115**, 4863–4868 (2018).
3. C. J. Wallace, M. Joshi, Comparison of land–ocean warming ratios in updated observed records and CMIP5 climate models. *Environ. Res. Lett.* **13**, 114011 (2018).
4. S. Manabe, R. J. Stouffer, M. J. Spelman, K. Bryan, Transient responses of a coupled ocean–atmosphere model to gradual changes of atmospheric CO_2. Part I. Annual mean response. *J. Clim.* **4**, 785–818 (1991).
5. M. M. Joshi, J. M. Gregory, M. J. Webb, D. M. H. Sexton, T. C. Johns, Mechanisms for the land/sea warming contrast exhibited by simulations of climate change. *Clim. Dyn.* **30**, 455–465 (2008).
6. M. P. Byrne, P. A. O'Gorman, Land-ocean warming contrast over a wide range of climates: Convective quasi-equilibrium theory and idealized simulations. *J. Clim.* **26**, 4000–4016 (2013).
7. M. P. Byrne, P. A. O'Gorman, Understanding decreases in land relative humidity with global warming: Conceptual model AND GCM simulations. *J. Clim.* **29**, 9045–9061 (2016).
8. O. Geoffroy, D. Saint-Martin, A. Voldoire, Land-sea warming contrast: The role of the horizontal energy transport. *Clim. Dyn.* **45**, 3493–3511 (2015).
9. M. P. Byrne, P. A. O'Gorman, Link between land-ocean warming contrast and surface relative humidities in simulations with coupled climate models. *Geophys. Res. Lett.* **40**, 5223–5227 (2013).
10. S. Sherwood, Q. Fu, A drier future? *Science* **343**, 737–739 (2014).
11. D. Rind, D. Peteet, Terrestrial conditions at the Last Glacial Maximum and CLIMAP sea-surface temperature estimates: Are they consistent? *Quat. Res.* **24**, 1–22 (1985).
12. S. Pinot, G. Ramstein, S. P. Harrison, I. C. Prentice, J. Guiot, M. Stute, S. Joussaume, Tropical paleoclimates at the Last Glacial Maximum: Comparison of Paleoclimate Modeling Intercomparison Project (PMIP) simulations and paleodata. *Clim. Dyn.* **15**, 857–874 (1999).
13. J. E. Tierney, J. Zhu, J. King, S. B. Malevich, G. J. Hakim, C. J. Poulsen, Glacial cooling and climate sensitivity revisited. *Nature* **584**, 569–573 (2020).
14. A. M. Seltzer, J. Ng, W. Aeschbach, R. Kipfer, J. T. Kulongoski, J. P. Severinghaus, M. Stute, Widespread six degrees Celsius cooling on land during the Last Glacial Maximum. *Nature* **593**, 228–232 (2021).
15. R. Pincus, P. M. Forster, B. Stevens, The Radiative Forcing Model Intercomparison Project (RFMIP): Experimental protocol for CMIP6 (Geoscientific Model Development, 2016); 10.5194/gmd-2016-88.
16. J. C. H. Chiang, The Tropics in Paleoclimate. *Annu. Rev. Earth Planet. Sci.* **37**, 263–297 (2009).
17. K. Lambeck, H. Rouby, A. Purcell, Y. Sun, M. Sambridge, Sea level and global ice volumes from the Last Glacial Maximum to the Holocene. *Proc. Natl. Acad. Sci. U.S.A.* **111**, 15296–15303 (2014).
18. E. J. Gowan, X. Zhang, S. Khosravi, A. Rovere, P. Stocchi, A. L. C. Hughes, R. Gyllencreutz, J. Mangerud, J. I. Svendsen, G. Lohmann, A new global ice sheet reconstruction for the past 80 000 years. *Nat. Commun.* **12**, 1199 (2021).
19. R. Chadwick, P. Good, K. Willett, A simple moisture advection model of specific humidity change over land in response to sst warming. *J. Clim.* **29**, 7613–7632 (2016).
20. W. Wagner, A. Pruß, The IAPWS formulation 1995 for the thermodynamic properties of ordinary water substance for general and scientific use. *J. Phys. Chem. Ref. Data Monogr.* **31**, 387–535 (2002).
21. M. A. Mélières, P. Martinerie, D. Raynaud, L. Lliboutry, Glacial-interglacial mean sea level pressure change due to sea level, ice sheet and atmospheric mass changes. *Glob. Planet. Change* **3**, 333–340 (1991).
22. M. Kageyama, S. P. Harrison, M. L. Kapsch, M. Lofverstrom, J. M. Lora, U. Mikolajewicz, S. Sherriff-Tadano, T. Vadsaria, A. Abe-Ouchi, N. Bouttes, D. Chandan, L. J. Gregoire, R. F. Ivanovic, K. Izumi, A. N. LeGrande, F. Lhardy, G. Lohmann, P. A. Morozova, R. Ohgaito, A. Paul, W. R. Peltier, C. J. Poulsen, A. Quiquet, D. M. Roche, X. Shi, J. E. Tierney, P. J. Valdes, E. Volodin, J. Zhu, The PMIP4 Last Glacial Maximum experiments: Preliminary results and comparison with the PMIP3 simulations. *Clim. Past.* **17**, 1065–1089 (2021).
23. P. H. Blard, J. Lavé, R. Pik, P. Wagnon, D. Bourlès, Persistence of full glacial conditions in the central Pacific until 15,000 years ago. *Nature* **449**, 591–594 (2007).
24. S. E. Loomis, J. M. Russell, D. Verschuren, C. Morrill, G. de Cort, J. S. Sinninghe Damsté, D. Olago, H. Eggermont, F. A. Street-Perrott, M. A. Kelly, The tropical lapse rate steepened during the Last Glacial Maximum. *Sci. Adv.* **3**, e1600815 (2017).
25. A. K. Tripati, S. Sahany, D. Pittman, R. A. Eagle, J. D. Neelin, J. L. Mitchell, L. Beaufort, Modern and glacial tropical snowlines controlled by sea surface temperature and atmospheric mixing. *Nat. Geosci.* **7**, 205–209 (2014).
26. K. Izumi, P. J. Bartlein, S. P. Harrison, Consistent large-scale temperature responses in warm and cold climates. *Geophys. Res. Lett.* **40**, 1817–1823 (2013).
27. G. A. Schmidt, J. D. Annan, P. J. Bartlein, B. I. Cook, E. Guilyardi, J. C. Hargreaves, S. P. Harrison, M. Kageyama, A. N. LeGrande, B. Konecky, S. Lovejoy, M. E. Mann, V. Masson-Delmotte, C. Risi, D. Thompson, A. Timmermann, L. B. Tremblay, P. Yiou, Using palaeo-climate comparisons to constrain future projections in CMIP5. *Clim. Past.* **10**, 221–250 (2014).
28. MARGO Project Members, Constraints on the magnitude and patterns of ocean cooling at the Last Glacial Maximum. *Nat. Geosci.* **2**, 127–132 (2009).
29. P. J. Bartlein, S. P. Harrison, S. Brewer, S. Connor, B. A. S. Davis, K. Gajewski, J. Guiot, T. I. Harrison-Prentice, A. Henderson, O. Peyron, I. C. Prentice, M. Scholze, H. Seppä, B. Shuman, S. Sugita, R. S. Thompson, A. E. Viau, J. Williams, H. Wu, Pollen-based continental climate reconstructions at 6 and 21 ka: A global synthesis. *Clim. Dyn.* **37**, 775–802 (2011).
30. S. F. Cleator, S. P. Harrison, N. K. Nichols, I. Colin Prentice, I. Roulstone, A new multivariable benchmark for Last Glacial Maximum climate simulations. *Clim. Past.* **16**, 699–712 (2020).
31. S. C. Sherwood, M. J. Webb, J. D. Annan, K. C. Armour, P. M. Forster, J. C. Hargreaves, G. Hegerl, S. A. Klein, K. D. Marvel, E. J. Rohling, M. Watanabe, T. Andrews, P. Braconnot, C. S. Bretherton, G. L. Foster, Z. Hausfather, A. S. von der Heydt, R. Knutti, T. Mauritsen, J. R. Norris, C. Proistosescu, M. Rugenstein, G. A. Schmidt, K. B. Tokarska, M. D. Zelinka, An assessment of Earth's climate sensitivity using multiple lines of evidence. *Geophysics* **58**, e2019RG000678 (2020).
32. A. Schmittner, N. M. Urban, J. D. Shakun, N. M. Mahowald, P. U. Clark, P. J. Bartlein, A. C. Mix, A. Rosell-Melé, Climate sensitivity estimated from temperature reconstructions of the Last Glacial Maximum. *Science* **334**, 1385–1388 (2011).
33. J. Zhu, B. L. Otto-Bliesner, E. C. Brady, C. J. Poulsen, J. E. Tierney, M. Lofverstrom, P. D. Nezio, Assessment of Equilibrium Climate Sensitivity of the Community Earth System Model

Version 2 through simulation of the Last Glacial Maximum. *Geophys. Res. Lett.* **48**, e2020GL091220 (2021).
34. V. Eyring, S. Bony, G. A. Meehl, C. A. Senior, B. Stevens, R. J. Stouffer, K. E. Taylor, Overview of the Coupled Model Intercomparison Project Phase 6 (CMIP6) experimental design and organization. *Geosci. Model Dev.* **9**, 1937–1958 (2016).
35. B. C. O'neill, C. Tebaldi, D. P. van Vuuren, V. Eyring, P. Friedlingstein, G. Hurtt, R. Knutti, E. Kriegler, J.-F. Lamarque, J. Lowe, G. A. Meehl, R. Moss, K. Riahi, B. M. Sanderson, The Scenario Model Intercomparison Project (ScenarioMIP) for CMIP6. *Geosci. Model Dev.* **9**, 3461–3482 (2016).
36. T. M. Merlis, M. Henry, Simple estimates of polar amplification in moist diffusive energy balance models. *J. Clim.* **31**, 5811–5824 (2018).
37. A. E. Putnam, W. S. Broecker, Human-induced changes in the distribution of rainfall. *Sci. Adv.* **3**, e1600871 (2017).
38. J. C. H. Chiang, C. M. Bitz, Influence of high latitude ice cover on the marine Intertropical Convergence Zone. *Clim. Dyn.* **25**, 477–496 (2005).
39. T. Schneider von Deimling, A. Ganopolski, H. Held, S. Rahmstorf, How cold was the Last Glacial Maximum? *Geophys. Res. Lett.* **33**, L14709 (2006).
40. J. D. Annan, J. C. Hargreaves, Using multiple observationally-based constraints to estimate climate sensitivity. *Geophys. Res. Lett.* **33**, L06704 (2006).
41. H. Hersbach, B. Bell, P. Berrisford, S. Hirahara, A. Horányi, J. Muñoz-Sabater, J. Nicolas, C. Peubey, R. Radu, D. Schepers, A. Simmons, C. Soci, S. Abdalla, X. Abellan, G. Balsamo, P. Bechtold, G. Biavati, J. Bidlot, M. Bonavita, G. Chiara, P. Dahlgren, D. Dee, M. Diamantakis, R. Dragani, J. Flemming, R. Forbes, M. Fuentes, A. Geer, L. Haimberger, S. Healy, R. J. Hogan, E. Hólm, M. Janisková, S. Keeley, P. Laloyaux, P. Lopez, C. Lupu, G. Radnoti, P. Rosnay, I. Rozum, F. Vamborg, S. Villaume, J. N. Thépaut, The ERA5 global reanalysis. *Q. J. Roy. Meteorol. Soc.* **146**, 1999–2049 (2020).
42. I. M. Held, B. J. Soden, Robust responses of the hydrological cycle to global warming. *J. Clim.* **19**, 5686–5699 (2006).
43. M. Adloff, C. H. Reick, M. Claussen, Earth system model simulations show different feedback strengths of the terrestrial carbon cycle under glacial and interglacial conditions. *Earth Syst. Dynam.* **9**, 413–425 (2018).
44. D. Sidorenko, T. Rackow, T. Jung, T. Semmler, D. Barbi, S. Danilov, K. Dethloff, W. Dorn, K. Fieg, H. F. Goessling, D. Handorf, S. Harig, W. Hiller, S. Juricke, M. Losch, J. Schröter, D. V. Sein, Q. Wang, Towards multi-resolution global climate modeling with ECHAM6––FESOM. Part I: Model formulation and mean climate. *Clim. Dyn.* **44**, 757–780 (2015).
45. G. Lohmann, M. Butzin, N. Eissner, X. Shi, C. Stepanek, Abrupt Climate and Weather Changes Across Time Scales. *Paleoceanogr. Paleoclimatol.* **35**, e2019PA003782 (2020).
46. E. M. Volodin, E. V. Mortikov, S. V. Kostrykin, V. Y. Galin, V. N. Lykossov, A. S. Gritsun, N. A. Diansky, A. V. Gusev, N. G. Iakovlev, A. A. Shestakova, S. V. Emelina, Simulation of the modern climate using the INM-CM48 climate model. *Russ. J. Numer. Anal. Math. Model.* **33**, 367–374 (2018).
47. P. Sepulchre, A. Caubel, J. B. Ladant, L. Bopp, O. Boucher, P. Braconnot, P. Brockmann, A. Cozic, Y. Donnadieu, J. L. Dufresne, V. Estella-Perez, C. Ethé, F. Fluteau, M. A. Foujols, G. Gastineau, J. Ghattas, D. Hauglustaine, F. Hourdin, M. Kageyama, M. Khodri, O. Marti, Y. Meurdesoif, J. Mignot, A. C. Sarr, J. Servonnat, D. Swingedouw, S. Szopa, D. Tardif, IPSL-CM5A2–An Earth system model designed for multi-millennial climate simulations. *Geosci. Model Dev.* **13**, 3011–3053 (2020).
48. W. R. Peltier, G. Vettoretti, Dansgaard-Oeschger oscillations predicted in a comprehensive model of glacial climate: A "kicked" salt oscillator in the Atlantic. *Geophys. Res. Lett.* **41**, 7306–7313 (2014).
49. D. Chandan, W. Richard Peltier, Regional and global climate for the mid-Pliocene using the University of Toronto version of CCSM4 and PlioMIP2 boundary conditions. *Clim. Past.* **13**, 919–942 (2017).
50. D. Chandan, W. Richard Peltier, On the mechanisms of warming the mid-Pliocene and the inference of a hierarchy of climate sensitivities with relevance to the understanding of climate futures. *Clim. Past.* **14**, 825–856 (2018).
51. T. Sueyoshi, R. Ohgaito, A. Yamamoto, M. O. Chikamoto, T. Hajima, H. Okajima, M. Yoshimori, M. Abe, R. O'ishi, F. Saito, S. Watanabe, M. Kawamiya, A. Abe-Ouchi, Set-up of the PMIP3 paleoclimate experiments conducted using an Earth system model, MIROC-ESM. *Geosci. Model Dev.* **6**, 819–836 (2013).
52. P. J. Valdes, E. Armstrong, M. P. S. Badger, C. D. Bradshaw, F. Bragg, M. Crucifix, T. Davies-Barnard, J. J. Day, A. Farnsworth, C. Gordon, P. O. Hopcroft, A. T. Kennedy, N. S. Lord, D. J. Lunt, A. Marzocchi, L. M. Parry, V. Pope, W. H. G. Roberts, E. J. Stone, G. J. L. Tourte, J. H. T. Williams, The BRIDGE HadCM3 family of climate models: HadCM3@Bristol v1.0. *Geosci. Model Dev.* **10**, 3715–3743 (2017).
53. F. Lhardy, N. Bouttes, D. M. Roche, X. Crosta, C. Waelbroeck, D. Paillard, Impact of Southern Ocean surface conditions on deep ocean circulation during the LGM: A model analysis. *Clim. Past.* **17**, 1139–1159 (2021).
54. G. Danabasoglu, NCAR CESM2 model output prepared for CMIP6 CMIP abrupt-4xCO2 (Earth System Grid Federation, 2019); 10.22033/ESGF/CMIP6.7519.
55. O. Boucher, O. Boucher, S. Denvil, G. Levavasseur, A. Cozic, A. Caubel, M.-A. Foujols, Y. Meurdesoif, Y. Balkanski, R. Checa-Garcia, D. Hauglustaine, S. Bekki, M. Marchand, IPSL IPSL-CM5A2-INCA model output prepared for CMIP6 CMIP abrupt-4xCO2 (Earth System Grid Federation, 2020); 10.22033/ESGF/CMIP6.13644.
56. K.-H. Wieners, M. Giorgetta, J. Jungclaus, C. Reick, M. Esch, M. Bittner, S. Legutke, M. Schupfner, F. Wachsmann, V. Gayler, H. Haak, P. de Vrese, T. Raddatz, T. Mauritsen, J.-S. von Storch, J. Behrens, V. Brovkin, M. Claussen, T. Crueger, I. Fast, S. Fiedler, S. Hagemann, C. Hohenegger, T. Jahns, S. Kloster, S. Kinne, G. Lasslop, L. Kornblueh, J. Marotzke, D. Matei, K. Meraner, U. Mikolajewicz, K. Modali, W. Müller, J. Nabel, D. Notz, K. Peters, R. Pincus, H. Pohlmann, J. Pongratz, S. Rast, H. Schmidt, R. Schnur, U. Schulzweida, K. Six, B. Stevens, A. Voigt, E. Roeckner, MPI-M MPI-ESM1.2-LR model output prepared for CMIP6 CMIP abrupt-4xCO2 (Earth System Grid Federation, 2019); 10.22033/ESGF/CMIP6.6459.
57. E. Volodin, E. Mortikov, A. Gritsun, V. Lykossov, V. Galin, N. Diansky, A. Gusev, S. Kostrykin, N. Iakovlev, A. Shestakova, S. Emelina, INM INM-CM4–8 model output prepared for CMIP6 CMIP abrupt-4xCO2 (Earth System Grid Federation, 2019); 10.22033/ESGF/CMIP6.4931.
58. T. Hajima, M. Abe, O. Arakawa, T. Suzuki, Y. Komuro, T. Ogura, K. Ogochi, M. Watanabe, A. Yamamoto, H. Tatebe, M. A. Noguchi, R. Ohgaito, A. Ito, D. Yamazaki, A. Ito, K. Takata, S. Watanabe, M. Kawamiya, K. Tachiiri, MIROC MIROC-ES2L model output prepared for CMIP6 CMIP abrupt-4xCO2 (Earth System Grid Federation, 2019): 10.22033/ESGF/CMIP6.5410.
59. J. Ridley, M. Menary, T. Kuhlbrodt, M. Andrews, T. Andrews, MOHC HadGEM3-GC31-LL model output prepared for CMIP6 CMIP abrupt-4xCO2 (Earth System Grid Federation, 2019); 10.22033/ESGF/CMIP6.5839.
60. T. Semmler, S. Danilov, T. Rackow, D. Sidorenko, D. Barbi, J. Hegewald, D. Sein, Q. Wang, T. Jung, AWI AWI-CM1.1MR model output prepared for CMIP6 CMIP abrupt-4xCO2 (Earth System Grid Federation, 2018); 10.22033/ESGF/CMIP6.2568.
61. P. A. Gopinathan, S. Narayanasetti, A. D. Choudhury, M. Singh, K. Raghavan, S. Panickal, A. Modi, CCCR-IITM IITM-ESM model output prepared for CMIP6 CMIP abrupt-4xCO2 (Earth System Grid Federation, 2019); 10.22033/ESGF/CMIP6.3516.
62. D. C. Bader, R. Leung, M. Taylor, R. B. McCoy, E3SM-Project E3SM1.0 model output prepared for CMIP6 CMIP abrupt-4xCO2 (Earth System Grid Federation, 2019); 10.22033/ESGF/CMIP6.4491.
63. Z. Song, F. Qiao, Y. Bao, Q. Shu, Y. Song, X. Yang, FIO-QLNM FIO-ESM2.0 model output prepared for CMIP6 CMIP abrupt-4xCO2 (Earth System Grid Federation, 2020); 10.22033/ESGF/CMIP6.9161.
64. Y. Yu, CAS FGOALS-f3-L model output prepared for CMIP6 CMIP abrupt-4xCO2 (Earth System Grid Federation, 2019); 10.22033/ESGF/CMIP6.3176.
65. N. C. Swart, J. N. S. Cole, V. V. Kharin, M. Lazare, J. F. Scinocca, N. P. Gillett, J. Anstey, V. Arora, J. R. Christian, Y. Jiao, W. G. Lee, F. Majaess, O. A. Saenko, C. Seiler, C. Seinen, A. Shao, L. Solheim, K. von Salzen, D. Yang, B. Winter, M. Sigmond, CCCma CanESM5 model output prepared for CMIP6 CMIP abrupt-4xCO2 (Earth System Grid Federation, 2019); 10.22033/ESGF/CMIP6.3532.
66. J. P. Krasting, J. G. John, C. Blanton, C. McHugh, S. Nikonov, A. Radhakrishnan, K. Rand, N. T. Zadeh, V. Balaji, J. Durachta, C. Dupuis, R. Menzel, T. Robinson, S. Underwood, H. Vahlenkamp, K. A. Dunne, P. P. G. Gauthier, P. Ginoux, S. M. Griffies, R. Hallberg, M. Harrison, W. Hurlin, S. Malyshev, V. Naik, F. Paulot, D. J. Paynter, J. Ploshay, B. G. Reichl, D. M. Schwarzkopf, C. J. Seman, L. Silvers, B. Wyman, Y. Zeng, A. Adcroft, J. P. Dunne, R. Dussin, H. Guo, J. He, I. M. Held, L. W. Horowitz, P. Lin, P. C. D. Milly, E. Shevliakova, C. Stock, M. Winton, A. T. Wittenberg, Y. Xie, M. Zhao, NOAA-GFDL GFDL-ESM4 model output prepared for CMIP6 CMIP abrupt-4xCO2 (Earth System Grid Federation, 2018); 10.22033/ESGF/CMIP6.8489.
67. NASA Goddard Institute for Space Studies (NASA/GISS), NASA-GISS GISS-E2.1H model output prepared for CMIP6 CMIP abrupt-4xCO2 (Earth System Grid Federation, 2019); 10.22033/ESGF/CMIP6.6977.
68. S. Park, J. Shin, SNU SAM0-UNICON model output prepared for CMIP6 CMIP abrupt-4xCO2 (Earth System Grid Federation, 2019); 10.22033/ESGF/CMIP6.7783.
69. Y. Kim, Y. Noh, D. Kim, M.-I. Lee, H. J. Lee, S. Y. Kim, D. Kim, KIOST KIOST-ESM model output prepared for CMIP6 CMIP abrupt-4xCO2 (Earth System Grid Federation, 2019); 10.22033/ESGF/CMIP6.5288.
70. J. Cao, B. Wang, NUIST NESMv3 model output prepared for CMIP6 CMIP abrupt-4xCO2 (Earth System Grid Federation, 2019); 10.22033/ESGF/CMIP6.8719.
71. M. Dix, D. Bi, P. Dobrohotoff, R. Fiedler, I. Harman, R. Law, C. Mackallah, S. Marsland, S. O'Farrell, H. Rashid, J. Srbinovsky, A. Sullivan, C. Trenham, P. Vohralik, I. Watterson, G. Williams, M. Woodhouse, R. Bodman, F. B. Dias, C. Domingues, N. Hannah, A. Heerdegen, A. Savita, S. Wales, C. Allen, K. Druken, B. Evans, C. Richards, S. M. Ridzwan, D. Roberts, J. Smillie, K. Snow, M. Ward, R. Yang, CSIRO-ARCCSS ACCESS-CM2 model output prepared for CMIP6 ScenarioMIP ssp585 (Earth System Grid Federation, 2019); 10.22033/ESGF/CMIP6.4332.

72. X. Xin, T. Wu, X. Shi, F. Zhang, J. Li, M. Chu, Q. Liu, J. Yan, Q. Ma, M. Wei, BCC BCC-CSM2MR model output prepared for CMIP6 ScenarioMIP ssp585 (Earth System Grid Federation, 2019); 10.22033/ESGF/CMIP6.3050.
73. N. C. Swart, J. N. S. Cole, V. V. Kharin, M. Lazare, J. F. Scinocca, N. P. Gillett, J. Anstey, V. Arora, J. R. Christian, Y. Jiao, W. G. Lee, F. Majaess, O. A. Saenko, C. Seiler, C. Seinen, A. Shao, L. Solheim, K. von Salzen, D. Yang, B. Winter, M. Sigmond, CCCma CanESM5-CanOE model output prepared for CMIP6 ScenarioMIP ssp585 (Earth System Grid Federation, 2019); 10.22033/ESGF/CMIP6.10276.
74. T. Lovato, D. Peano, M. Butenschön, CMCC CMCC-ESM2 model output prepared for CMIP6 ScenarioMIP ssp585 (Earth System Grid Federation, 2021); 10.22033/ESGF/CMIP6.13259.
75. A. Voldoire, CNRM-CERFACS CNRM-CM6–1-HR model output prepared for CMIP6 ScenarioMIP ssp585 (Earth System Grid Federation, 2019); 10.22033/ESGF/CMIP6.4225.
76. Y. Yu, CAS FGOALS-f3-L model output prepared for CMIP6 ScenarioMIP ssp585 (Earth System Grid Federation, 2019); 10.22033/ESGF/CMIP6.3502.
77. Z. Song, F. Qiao, Y. Bao, Q. Shu, Y. Song, X. Yang, FIO-QLNM FIO-ESM2.0 model output prepared for CMIP6 ScenarioMIP ssp585 (Earth System Grid Federation, 2019); 10.22033/ESGF/CMIP6.9214.
78. P. Good, MOHC HadGEM3-GC31-LL model output prepared for CMIP6 ScenarioMIP ssp585 (Earth System Grid Federation, 2020); 10.22033/ESGF/CMIP6.10901.
79. S. Panickal, J. N. S. Cole, V. V. Kharin, M. Lazare, J. F. Scinocca, N. P. Gillett, J. Anstey, V. Arora, J. R. Christian, Y. Jiao, W. G. Lee, F. Majaess, O. A. Saenko, C. Seiler, C. Seinen, A. Shao, L. Solheim, K. von Salzen, D. Yang, B. Winter, M. Sigmond, CCCR-IITM IITM-ESM model output prepared for CMIP6 ScenarioMIP ssp585 (Earth System Grid Federation, 2020); 10.22033/ESGF/CMIP6.14753.
80. E. Volodin, E. Mortikov, A. Gritsun, V. Lykossov, V. Galin, N. Diansky, A. Gusev, S. Kostrykin, N. Iakovlev, A. Shestakova, S. Emelina, INM INM-CM5–0 model output prepared for CMIP6 ScenarioMIP ssp585 (Earth System Grid Federation, 2019); 10.22033/ESGF/CMIP6.12338.
81. Y. Kim, Y. Noh, D. Kim, M.-I. Lee, H. J. Lee, S. Y. Kim, D. Kim, KIOST KIOST-ESM model output prepared for CMIP6 ScenarioMIP ssp585 (Earth System Grid Federation, 2019); 10.22033/ESGF/CMIP6.11249.
82. H. Shiogama, M. Abe, H. Tatebe, MIROC MIROC6 model output prepared for CMIP6 ScenarioMIP ssp585 (Earth System Grid Federation, 2019); 10.22033/ESGF/CMIP6.5771.
83. K. Tachiiri, M. Abe, T. Hajima, O. Arakawa, T. Suzuki, Y. Komuro, K. Ogochi, M. Watanabe, A. Yamamoto, H. Tatebe, M. A. Noguchi, R. Ohgaito, A. Ito, D. Yamazaki, A. Ito, K. Takata, S. Watanabe, M. Kawamiya, MIROC MIROC-ES2L model output prepared for CMIP6 ScenarioMIP ssp585 (Earth System Grid Federation, 2019); 10.22033/ESGF/CMIP6.5770.
84. S. Yukimoto, T. Koshiro, H. Kawai, N. Oshima, K. Yoshida, S. Urakawa, H. Tsujino, D. Deushi, T. Tanaka, M. Hosaka, H. Yoshimura, E. Shindo, R. Mizuta, M. Ishii, A. Obata, Y. Adachi, MRI MRI-ESM2.0 model output prepared for CMIP6 ScenarioMIP ssp585 (2019); 10.22033/ESGF/CMIP6.6929.
85. D. J. L. Oliviè, Ø. Seland, T. Toniazzo, A. Gjermundsen, L. S. Graff, J. B. Debernard, A. K. Gupta, Y. He, A. Kirkevåg, J. Schwinger, J. Tjiputra, K. S. Aas, I. Bethke, Y. Fan, J. Griesfeller, A. Grini, C. Guo, M. Ilicak, I. H. H. Karset, O. A. Landgren, J. Liakka, K. O. Moseid, A. Nummelin, C. Spensberger, H. Tang, Z. Zhang, C. Heinze, T. Iversen, M. Schulz, NCC NorESM2-MM model output prepared for CMIP6 ScenarioMIP ssp585 (Earth System Grid Federation, 2019); 10.22033/ESGF/CMIP6.8321.
86. W.-L. Lee, H.-C. Liang, AS-RCEC TaiESM1.0 model output prepared for CMIP6 ScenarioMIP ssp585 (Earth System Grid Federation, 2020); 10.22033/ESGF/CMIP6.9823.
87. G. Danabasoglu, NCAR CESM2 model output prepared for CMIP6 ScenarioMIP ssp585 (Earth System Grid Federation, 2019); 10.22033/ESGF/CMIP6.7768.
88. W. Huang, THU CIESM model output prepared for CMIP6 ScenarioMIP ssp585 (Earth System Grid Federation, 2020); 10.22033/ESGF/CMIP6.8863.
89. T. Lovato, D. Peano, CMCC CMCC-CM2-SR5 model output prepared for CMIP6 ScenarioMIP ssp585 (Earth System Grid Federation, 2020); 10.22033/ESGF/CMIP6.3896.
90. A. Voldoire, CNRM-CERFACS CNRM-CM6–1 model output prepared for CMIP6 ScenarioMIP ssp585 (Earth System Grid Federation, 2019); 10.22033/ESGF/CMIP6.4224.
91. A. Voldoire, CNRM-CERFACS CNRM-ESM2–1 model output prepared for CMIP6 ScenarioMIP ssp585 (Earth System Grid Federation, 2019); 10.22033/ESGF/CMIP6.4226.
92. D. C. Bader, R. Leung, M. Taylor, R. B. McCoy, E3SM-Project E3SM1.1 model output prepared for CMIP6 ScenarioMIP ssp585 (Earth System Grid Federation, 2020); 10.22033/ESGF/CMIP6.15179.
93. E.-E. C. (EC-Earth), EC-Earth-Consortium EC-Earth3-CC model output prepared for CMIP6 ScenarioMIP ssp585 (Earth System Grid Federation, 2021); 10.22033/ESGF/CMIP6.15636.
94. L. Li, CAS FGOALS-g3 model output prepared for CMIP6 ScenarioMIP ssp585 (Earth System Grid Federation, 2019); 10.22033/ESGF/CMIP6.3503.
95. J. G. John, C. Blanton, C. McHugh, A. Radhakrishnan, K. Rand, H. Vahlenkamp, C. Wilson, N. T. Zadeh, J. P. Dunne, R. Dussin, L. W. Horowitz, J. P. Krasting, P. Lin, S. Malyshev, V. Naik, J. Ploshay, E. Shevliakova, L. Silvers, C. Stock, M. Winton, Y. Zeng, NOAA-GFDL GFDL-ESM4 model output prepared for CMIP6 ScenarioMIP ssp585 (Earth System Grid Federation, 2018); 10.22033/ESGF/CMIP6.8706.
96. L. Jackson, MOHC HadGEM3-GC31-MM model output prepared for CMIP6 ScenarioMIP ssp585 (Earth System Grid Federation, 2020); 10.22033/ESGF/CMIP6.10902.
97. E. Volodin, E. Mortikov, A. Gritsun, V. Lykossov, V. Galin, N. Diansky, A. Gusev, S. Kostrykin, N. Iakovlev, A. Shestakova, S. Emelina, INM INM-CM4–8 model output prepared for CMIP6 ScenarioMIP ssp585 (Earth System Grid Federation, 2019); 10.22033/ESGF/CMIP6.12337.
98. Y.-H. Byun, Y.-J. Lim, S. Shim, H. M. Sung, M. Sun, J. Kim, B.-H. Kim, J.-H. Lee, H. Moon, NIMS-KMA KACE1.0-G model output prepared for CMIP6 ScenarioMIP ssp585 (Earth System Grid Federation, 2019); 10.22033/ESGF/CMIP6.8456.
99. R. Stouffer, UA MCM-UA-1-0 model output prepared for CMIP6 ScenarioMIP ssp585 (Earth System Grid Federation, 2019); 10.22033/ESGF/CMIP6.13901.
100. K.-H. Wieners, M. Giorgetta, J. Jungclaus, C. Reick, M. Esch, M. Bittner, V. Gayler, H. Haak, P. de Vrese, T. Raddatz, T. Mauritsen, J.-S. von Storch, J. Behrens, V. Brovkin, M. Claussen, T. Crueger, I. Fast, S. Fiedler, S. Hagemann, C. Hohenegger, T. Jahns, S. Kloster, S. Kinne, G. Lasslop, L. Kornblueh, J. Marotzke, D. Matei, K. Meraner, U. Mikolajewicz, K. Modali, W. Müller, J. Nabel, D. Notz, K. Peters, R. Pincus, H. Pohlmann, J. Pongratz, S. Rast, H. Schmidt, R. Schnur, U. Schulzweida, K. Six, B. Stevens, A. Voigt, E. Roeckner, MPI-M MPI-ESM1.2-LR model output prepared for CMIP6 ScenarioMIP ssp585 (Earth System Grid Federation, 2019); 10.22033/ESGF/CMIP6.6705.
101. Ø. Seland, M. Bentsen, D. J. L. Oliviè, T. Toniazzo, A. Gjermundsen, L. S. Graff, J. B. Debernard, A. K. Gupta, Y. He, A. Kirkevåg, J. Schwinger, J. Tjiputra, K. S. Aas, I. Bethke, Y. Fan, J. Griesfeller, A. Grini, C. Guo, M. Ilicak, I. H. H. Karset, O. A. Landgren, J. Liakka, K. O. Moseid, A. Nummelin, C. Spensberger, H. Tang, Z. Zhang, C. Heinze, T. Iversen, M. Schulz, NCC NorESM2-LM model output prepared for CMIP6 ScenarioMIP ssp585 (Earth System Grid Federation, 2019); 10.22033/ESGF/CMIP6.8319.
102. S. Shim, Y.-J. Lim, Y.-H. Byun, J. Seo, S. Kwon, B.-H. Kim, NIMS-KMA UKESM1.0-LL model output prepared for CMIP6 ScenarioMIP ssp585 (Earth System Grid Federation, 2021); 10.22033/ESGF/CMIP6.8457.

Acknowledgments: We are grateful for the development of the TA theory (by M. Joshi, M. Byrne, P. O'Gorman, R. Sutton and others) that inspired this analysis and to the paleoceanographic and paleoclimate communities for the generation of high-quality records included in the compilations that enabled this work. We thank D. Bekaert for graphic design help with Fig. 1 and J. Severinghaus for helpful conversations that motivated this analysis. J.-Y. Peterschmitt is thanked for the help with preparing and making the PMIP4 data accessible at http://dods.lsce.ipsl.fr/pmip4/db. We acknowledge the World Climate Research Programme, which, through its Working Group on Coupled Modelling (WCRP), coordinated and promoted CMIP6, and the Paleoclimate Modelling Intercomparison Project [PMIP; supported by WCRP and the Past Global Changes (PAGES) programme] for coordinating the LGM experiments. We thank the climate modeling groups for producing and making available their model output, the Earth System Grid Federation (ESGF) for archiving the data and providing access, and the multiple funding agencies who support CMIP6, PMIP, and ESGF. The results shown here use the 2022-10-19 versions of the CMIP6 and PMIP4 databases. **Funding:** This study was supported by the NSF-EAR award no. 2102457 (to A.M.S.). M.K. and P.-H.B. are funded by CNRS. **Author contributions:** All authors contributed to conceptualization, methodology, and investigation in this study. A.M.S. wrote the original draft and performed the formal analysis, M.K. curated paleoclimate model data, and all authors contributed to review and editing. **Competing interests:** The authors declare that they have no competing interests. **Data and materials availability:** All data needed to evaluate the conclusions in the paper are present in the paper and/or the Supplementary Materials. In particular, model results for low-latitude mean land surface and sea surface temperature change are available in tables S1 to S3, along with references to individual CMIP6/PMIP4 models. PMIP4 LGM results were made available by Kageyama *et al.* (*22*) (http://dods.lsce.ipsl.fr/pmip4/db), CMIP6 abrupt-4×CO_2 results were accessed from the Woods Hole Oceanographic Institution CMIP6 database, and CMIP6 SSP5-8.5 results were accessed from the Climate Data Store (https://cds.climate.copernicus.eu).

Submitted 15 November 2022
Accepted 10 January 2023
Published 8 February 2023
10.1126/sciadv.adf8119